

Abstract

Acknowledgements

Contents

Chapter 1

Coupling between spin and strain density waves

1.1 Introduction

Chromium is an itinerant antiferromagnetic metal. It is the hallmark example of a material where a SDW develops due to local repulsive interactions of the electron gas, combined with a nesting of the fermi surface.

1.2 Experimental methods

Before focusing on the theoretical description of the coupling between the SDW and CDW, we take a look at the experimental techniques and results that we are seeking to reproduce. Optical pulses were used to heat up the material, mostly absorbed by the SDW order through photoexcitation. An x-ray free-electron laser (XFEL) is then used to probe the bragg-peaks of the CDW and how they change in time. The need of the XFEL can be attributed to the very short timescales at which the observed behavior is exhibited by the material, with resolutions of a couple femtoseconds being made accessible. The scattering intensity of the bragg peak is directly proportional to the magnitude of the CDW, offering both phase and amplitude information of the oscillation that we study. It is important to realize that the SDW order is not directly accessible through these kinds of measurements, so we are effectively studying the effect of exciting one order parameter through the reaction of the other due to the coupling between them. XFELs also allow for higher peak selectivity (narrow and intense satellite Bragg peaks), such that it allows for measurements performed on thin films even deposited on thick substrates, as was the case in the experiments performed by A. Singer et.al. The thin films offer a clarity in terms of describing the physics of this process, since it leads to a very even excitation of the entire volume, and it causes the order parameters to be homogeneous throughout the material. This absence of topological defects is confirmed by the absence of a widening of the satellite peak associated with the PLD, as compared with the peaks of the material itself. [not sure about this, I actually don't understand what they are talking about in the paper either]. To this end,

a 30nm thick Cr film was used in the experiments, harboring seven periods of the SDW perpendicular to the plane. This thinness of the film also decreases the Neel temperature to 290K, from the bulk value of around 307K. The pulses used to excite the SDW were 40 fs long, with a total intensity of 2.9 mJ/cm^2 . In the experiments with two sequential pulses the power of the second pulse was roughly half that of the first.

1.3 Theory

[some explanation of Peierls instabilities etc, the things that cause the SDW in the first place?]

The geometry that is used in the experiment is such that a microscopic model as described above is unnecessary to describe the essential physics, since the Cr thin film can be considered to be homogeneous throughout the experiment. This allows us to instead adopt a continuum description utilizing a standard Landau theory with two order parameters describing the SDW (L) and PLD (y) and a coupling between them to describe the magnetostriction.

$$F = \frac{\alpha}{2}(T_L - T_c)L^2 + \frac{\beta}{4}L^4 - gL^2y + \frac{\omega_0}{2}y^2 + \frac{b}{4}y^4. \quad (1.1)$$

The double well potential that leads to the SDW is characterised by α and β , with the temperature of the SDW given by T_L , with the critical temperature T_c below which the phase transition occurs and the SDW order sets in. The coupling between the two order parameters is given by term with γ . Only even orders of L appear in the energy, since the energy is time reversal even, but L is time reversal odd. Notice, also, that the PLD order parameter y by itself would have a zero equilibrium value, the fourth order term with strength b is only included to provide a better fit to some anisotropic features of the experiment, not to bound the energy as is required if y would also undergo a second order phase transition as L . The equilibrium value of y will, however, be shifted away from zero due to the force applied to it by the nonzero equilibrium value of L , a key feature of this model to bear in mind for later. y is thus a pure slave order parameter.

The temperature of the SDW T_L is described by a two temperature model, including a time-dependent heat source describing the XFEL pulses, and a bath with non infinite mass and temperature T_b , meaning that the bath temperature will increase.

$$c_L \dot{T}_L = -k(T_L - T_b) + q(t) \quad (1.2)$$

$$c_b \dot{T}_b = -k(T_b - T_L) \quad (1.3)$$

where c_L, c_b are the heat capacities of the SDW and the bath, k the heat transfer rate, and $q(t)$ signifies the heat injected into the system through the photon pulses, and is modeled by a gaussian $q(t) = \frac{f}{\tau\sqrt{\pi}}e^{-(t-t_0)^2/2\tau^2}$, where τ denotes the pulse width. The dots signify time derivatives.

In order to solve the time evolution of the system we start by incorporating the free energy given by Eq. ?? into the full Lagrangian

$$\mathcal{L} = \frac{m_L(\dot{L} + \gamma_L L)^2}{2} + \frac{m_y(\dot{y} + \gamma_y y)^2}{2} - F, \quad (1.4)$$

where the γ denote the damping parameters for both order parameters. This then leads to the well-known Euler-Lagrange equations given by

$$m_L \ddot{L} = -\alpha(T - T_c)L - \beta L^3 + 2gLy - \gamma_L \dot{L} \quad (1.5)$$

$$m_y \ddot{y} = gL^2 - \omega_0^2 y - b y^3 - \gamma_y \dot{y} \quad (1.6)$$

which we then solve numerically to get the time evolution of both order parameters.

1.4 Results

The experimental results we use as a basis to fit our model to are shown in Fig. ???. In the numerical model, we found in earlier trials that the dynamics of the SDW order parameter L is orders of magnitude faster than the ones from the PLD y , as expected. This can also be seen from Fig. ?? since the energy potential is a lot flatter for y than for L , leading to a slower time evolution. This difference in dynamics makes it extremely hard to solve the differential equations numerically, we therefore assumed that at each timestep the L order parameter is in equilibrium in its instantaneous energy potential. This is equivalent to the limit of the mass m_L in Eq. ?? going to zero. The value of L at a given T_L and y can be found by minimizing the Landau free energy ?? in terms of L such that $\frac{\partial F}{\partial L} = 0$, leading to:

$$L_0 = \pm \sqrt{\frac{\alpha(T_L - T_c) + 2gy}{\beta}}. \quad (1.7)$$

This eliminates to evaluate Eq. ??, instead using Eq. ?? to evaluate L in the partial differential equation for the evolution of y .

We then took eleven representative experiments, which can be thought of as horizontal slices of Fig. ??(a), in order to fit the model parameters to get the best total fit across all datasets. The parameters are

$$\alpha = 6039, \beta = 7.97 \times 10^7, g = 0.52, \gamma_L = 25.0, \quad (1.8)$$

$$\omega_0 = 14.1, b = 3.38 \times 10^8, \gamma_y = 0.76, \quad (1.9)$$

$$f = 64.43, c_b = 3.58, c_L = 0.36, k = 1.29, \tau = 0.074 \quad (1.10)$$

The results of this fitting procedure is shown in Fig. ??, showing an excellent agreement between the theory and experiment.

To get a deeper understanding of the underlying effect, we look at the evolution of the free energy surfaces for both order parameters, as shown in Fig. ???. The characteristic double well potential for $L \neq 0$ equilibrium is clearly visible, and as expected, when the pulses hit and T_L increases in the term $\alpha(T_L - T_c)L^2$ of Eq. ??, we see that the potential flattens causing the the minimum of L to very quickly change, as discussed above. This in turn causes the single-well potential of y to shift as quickly. The dynamics of y is orders of magnitude slower than that of L and due to this instant shift of the energy surface, it will cause an oscillation of y . While the temperature T_L decreases again, L and the minimum of the y potential shift back towards the original equilibrium position. The oscillation of y remains for a relatively long time while this shift is occurring

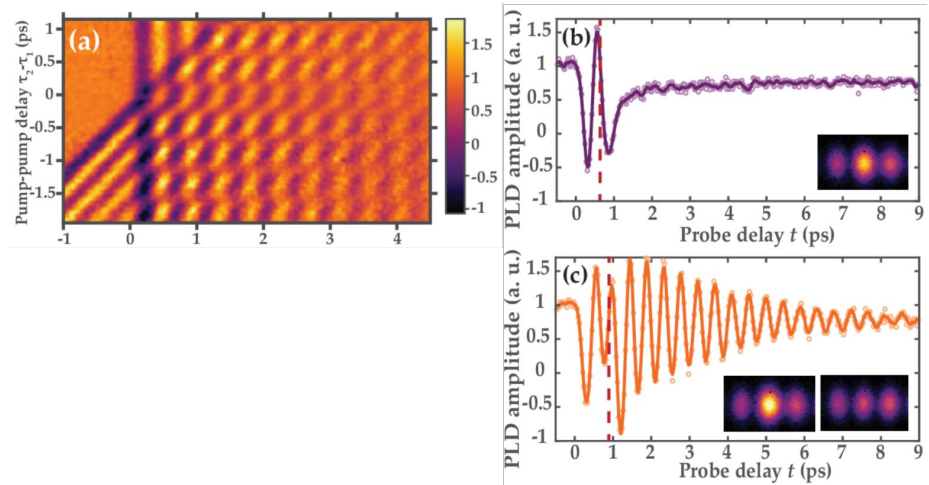


Figure 1.1: Experimental measurements. (a) Heatmap showing different pump-pump delay experiments. Notice the low intensity horizontal band around 0 ps pump-pump delay, where the oscillation amplitude is not at the maximum due to only one big pulse exciting the material and heating it through the phase transition, thus wasting a portion of the energy. The horizontal bands with alternating maximum and minimum magnitudes highlight constructive and destructive interference. (b-c), Magnitude of the strain wave in two extreme control cases, where (b) showcases maximum destructive interference, and (c) close to maximum constructive interference. Solid lines are experimental data (empty circles in figure) smoothed by a Savitzky-Golay filter. b – pump-pump delay of 620 fs, c – pump-pump delay of 845 fs.

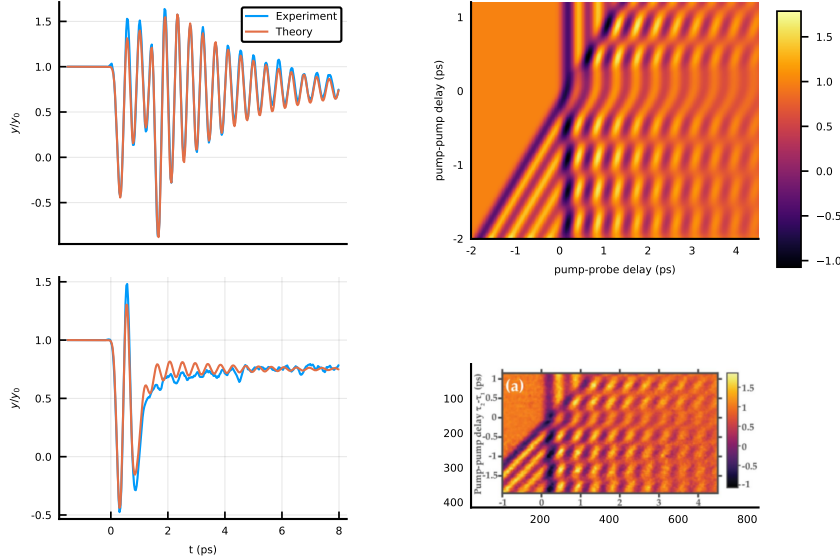


Figure 1.2: Comparison of theoretical fit vs Experiment. (a-b) Two examples of fits to constructive (a) and destructive (b) experiments. (c-d) Comparison of the theoretically generated heatmap (c) with the experimental heatmap (d).

since the damping is not that big (of the order of 4ps). It then becomes clear that if the second pulse can repeat this mechanism while the oscillation of y is still there, it can be increased or decreased depending on the timing. Having this understanding, let's investigate what the ideal way to excite y is.

First of all, when the system is relatively close to the phase transition of L , a small increase of temperature causes a large change in the value of L as shown through Eq. ??, and thus causes a large shift of the potential for y . It is then important to keep this initial shift of the potential for y in place until y crosses the minimum, converting as much potential energy into "kinetic" energy. This requires L to be heated slightly above the PT, which leads to the largest possible shift of the potential of y , and the additional temperature of L above T_c , together with the non-infinite cooling rate, allows y to gain the maximum kinetic energy. Since only the size of L matters for the potential surface of y , it can only cause a shift in one direction, meaning that, similar to someone pushing a swing, the ideal intervals for the subsequent pulses are close to multiples of the period of y , if the goal is maximum oscillation amplitude. The amount of periods depends on the cooling rate of L , this influences how much T_L can cool back down within one period and thus the size of the maximum shift, since this depends on distance of T_L from T_c , and the damping of y since that is the main source of kinetic energy loss. Taking these understandings into consideration, a high degree of control of the oscillation of y can be achieved through the intensity, amount and timing of a pulse train applied to the material. To demonstrate this, we went one step further and utilized the fitted model to simulate what pulse train has to be applied to the material in order for the oscillation maxima to follow a given envelope signal. To limit the dimensionality of the manifold of

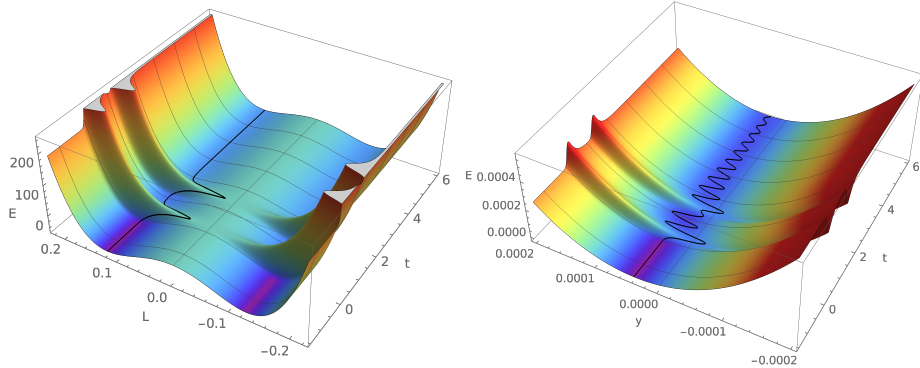


Figure 1.3: Time evolution of the energy surfaces of the order parameters.

possible solutions, we performed the following ruleset:

- Only one fluence can be used per pulse
- Pulses are grouped in sets per period of oscillation
- The first pulse group only has a single pulse, applied 20 fs after the first non zero value of the envelope function, this determines the fluence of each pulse
- The maximum allowed pulses per group is fixed
- The groups are then fitted sequentially, since the later pulses don't influence the oscillation caused by the earlier ones
- If the function is seen to increase during a period, the pulses will be initiated close to the ideal boost location, and if a decrease is required, close to the ideal brake location

Adhering to these rules, we tested this procedure on different envelope functions, showcased in Fig. ???. One assumption made here was that the heat capacity of the bath c_b was increased to infinity, this is done because with the increase of temperature of the bath, the equilibrium position of L changes and leads to a general downwards slope of the oscillation of y as see from panel (a-b) of Fig. ???.

Having fit the model, we can go one step further and try to fit the PLD oscillation to an arbitrary signal shape. To this end we use the fitted model, and predict the timing of a fixed fluence pulse train that will result in the required shape. The results are shown in Fig. ???. This showcases that with an arbitrary pulse train we can achieve indirect, but optimal control of the PLD order parameter.

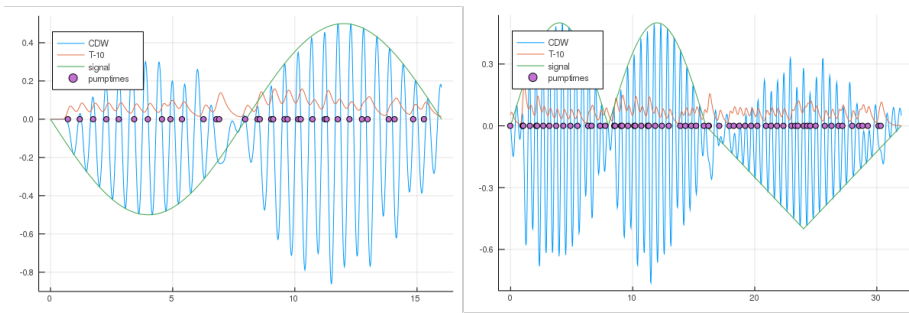


Figure 1.4: Two examples of optimal control. (a) Shows a reproduction of a sinusoidal envelope function, (b) shows the result for more complicated envelope, with an the absolute value of a sinusoidal followed by a half a period of a sawtooth function. The pulse train is highlighted by the purple dots, and the evolution of the temperature of the SDW is given by the orange plot.

Chapter 2

Magnetoelectric crankshaft: topologically protected switching in multiferroic GdMn_2O_5

2.1 Introduction

Efficient control and probing of robust order has historically been one of the main technological drivers for research in condensed matter. The hallmark example is the impact that the discovery of giant magnetoresistance has had on the efficiency of the readhead in hard disks. This is achieved by having the readhead be comprised of a multilayer sandwich composed of one pinned magnet, a non-magnetic metal and a soft magnet, the last of which aligns with the information storing magnetic domain on the disk itself. This will influence the amount of current which flows through the readhead depending on the alignment between the magnetizations in the two magnetic layers. This is because, due to the Stoner effect, the conducting states located close to the Fermi level of metallic magnets have a spin polarization along the internal magnetization. This causes the current carriers that exit the pinned magnet to be scattered strongly (leading to low conductivity) from the second magnet if the magnetizations are antiparallel, compared to when the two magnetizations are aligned (high conductivity). This leads to a change in current through the readhead, and can be electrically probed, indirectly reading out the magnetization state of the information storing domains underneath the readhead. The end result is a purely electrical way of reading the stored information, greatly increasing the efficiency compared with reading through induction in a solenoid.

There remains, however, the issue of writing the information in the first place. In modern state-of-the art high density storage technologies, this is still done by applying an external magnetic field with an electromagnet to reorient the ferromagnetic domains. One can imagine this to be quite an inefficient process, both from the point of view of granularity (stray fields and non-locality of the magnetic fields limit the minimum size of the domains) as from that

of dissipation. Improving these figures of merit drives much of the current research in the field of spintronics, with promising applications like spin-transfer torque devices, utilizing an inverse effect to the one described above in which the information is written to the ferromagnetic domains through the torque applied by the misaligned spin moments of polarized current carriers. This circumvents the need to create a magnetic field from circular currents in electromagnets.

It is clear that the longevity associated with magnetic order, combined with the ease of manipulation provided by charge-based order is highly desirable. This leads us to the topic of this chapter, namely the magnetoelectric effect in multiferroic insulators. As the name implies, the magnetoelectric effect allows for the electric control of magnetic order or the magnetic control of ferroelectric polarization [**Spaldin2019**, **Khomskii2009**, **Fiebig2005**, **Fiebig2016**, **Cheong2007**], the former of which is most attractive from a technological point of view.

In practice, however, there are many issues that limit the effectiveness of this cross-order coupling, and the number of multiferroic materials is limited to begin with. This latter point can be partly understood from a symmetry point of view. Namely, ferroelectric materials break inversion symmetry, whereas magnetic order needs the breaking of time reversal symmetry. There are thus only 13 Shubnikov magnetic point groups that allow simultaneous appearance of ferroelectricity and magnetization [**Wang2009**], but not all compounds that belong to one of those 13 groups showcase multiferroicity. Another reason for the relative rarity of multiferroic materials is that, generally speaking, ferroelectricity and magnetism are not compatible on the single ion level, i.e. they require ions with different valence configurations [**Spaldin2019**]. For example, among perovskites (ABO_3 , A cation, B anion), there are many ferroelectric or magnetic oxides, but the combination of the two is very uncommon. The reason in this case is that, in general, a prerequisite for ferroelectricity is a valence configuration of d^0 , i.e. an empty d -shell, or the presence of lone pairs (ns^2). Conversely, magnetism requires partially filled d or f shells, such that the unpaired electrons lead to nonzero magnetic moments on the constituent ions. These two requirements are mutually exclusive and can thus not be realized simultaneously on a single ion, making multiferroics not commonplace [there is also the issue of hybridization where empty shells lead to occupation of bonding orbitals and half-filled orbitals engaging in anti-bonding hybridization never stabilizing the ionic shift, not sure if I should also discuss that].

There are two ways around this issue, which lead to so-called Type-I and Type-II classification of multiferroics [**Khomskii2009**]. The Type-I variety harbors two different ‘subsystems’ that separately handle the magnetic and ferroelectric orders. Using perovskites again as an example, a ferroelectrically active A-site cation such as Bi^{3+} or Pb^{3+} can be combined with a magnetically active B-site anion such as Fe or Mn, as e.g. in BiMnO_3 . In this material, the lone pairs of the Bi ions result in a ferroelectric polarization of $\approx 16 \mu\text{C}/\text{cm}^2$, whereas the Mn ions result in a ferromagnetic phase below 110K [**Wang2009**]. One can write down a Landau Theory for a homogeneous type-II multiferroic

by expanding the free energy F in terms of P and magnetization M :

$$F(P, H) = F_0 + \frac{a}{2}(T - T_P)P^2 + \frac{b}{4}P^4 - PE \quad (2.1)$$

$$+ \frac{\alpha}{2}(T - T_M)M^2 + \frac{\beta}{4}M^4 - MH - \frac{g}{2}P^2M^2. \quad (2.2)$$

This is the simplest form of the free energy of a multiferroic with ferroelectric polarization P and magnetization M . All parameters are taken to be positive, such that below the ferroelectric (ferromagnetic) transition temperature T_P (T_M) nonzero P (M) develops. The lowest symmetrically allowed magnetoelectric term that couples P and M is $-gP^2M^2$, obeying both time and inversion symmetries above the transition temperatures T_P and T_M . Minimizing the energy with respect to both orders for $T < T_M, T_P$, with no applied external fields, leads to

$$P^2 = -a(T - T_P)/b + gM^2 \quad (2.3)$$

$$M^2 = -\alpha(T - T_M)/\beta + gP^2. \quad (2.4)$$

Both order parameters thus depend on the value of the other through the magnetoelectric coupling g . This leads to a change in one through an applied perturbation to the other. The different origin of both orders, however, usually results in a small value of g . Indeed, the effective dielectric constant ε of BiMnO₃ only displays a weak anomaly at the ferromagnetic transition temperature, and is only weakly affected by an external magnetic field, leading to a variation of 0.6% of ε at a field value of 9T.

The other class of multiferroics, i.e. those with Type-II multiferroicity, generally hold a bigger magnetoelectric effect, because the magnetic and ferroelectric orders both originate from the same underlying physics.

These multiferroics have improper ferroelectricity, i.e. the electron degrees of freedom cause a particular magnetic configuration that breaks inversion symmetry, rather than a structural instability through phonon instabilities and the structural deformations associated with them. To optimize the magnetic exchange energies, however, there will be displacements of the ions, that ultimately leads to a lowering of the crystalline symmetry. Although the size of the electric polarization thus created is usually orders of magnitude smaller than in Type-I multiferroics, the common origin of the two orders leads to a very sizable magnetoelectric effect.

Here we specifically investigate GdMn₂O₅ (see Fig. ??) [Khomskii2009], showing an exceptional tunability of the ferroelectric polarization through an applied magnetic field [Lee13]. The orthorhombic RMn₂O₅ manganites all have a very complex crystalline structure, which leads to a wealth of different phases depending on the temperature, rare-earth, external magnetic field and even electric-field poling history [Zheng2019]. To keep the discussion tractable and in line with the experiments that were performed, we give a summary of the transitions and phases that are important for this part of the Thesis. RMn₂O₅ have crystallographic group *Pbam* [Alonso97] in the paramagnetic phase at high temperature, which eventually gets lowered to the crystallographic space group *Pab21a* when the commensurate magnetic order locks in below $T_N \sim 33K$. This order is characterised by the propagation vector $\mathbf{k} = (1/2, 0, 0)$, i.e. there is a unit cell doubling along the crystalline *a*-direction. Spins are ordered

ferromagnetically along the crystalline c -direction. This magnetic transition goes hand in hand with a sharp anomaly in the dielectric constant ε_b , signalling the onset of the improper ferroelectric polarization order along the b -direction [Lee13]. When the temperature is lowered further, the polarization P_b saturates to a maximum value of around $3600 \mu\text{C}/\text{m}^2$, which is the largest of all rare-earth magnanites, but still tiny compared to proper ferroelectrics like BaTiO₃ with $P \approx 2 \times 10^5 \mu\text{C}/\text{m}^2$. The magnetic configuration features two AFM Mn chains per unit cell, which are formed by pyramidal coordinated Mn³⁺ and octahedrally coordinated Mn⁴⁺ ions, as indicated by the light blue lines and purple polygons in Fig. ???. The Mn spins of the chains in GdMn₂O₅ lie mostly along the fourfold symmetry axis of the Mn pyramids, making angles of $\pm 23.4^\circ$ with the a -axis.

The improper ferroelectricity is generated through the symmetric Heisenberg exchange striction, combined with the geometric frustration and strong antiferromagnetic exchanges [Choi2008]. The geometric frustration appears due to the odd number of AFM coupled spins in the Mn pentagons that surround each Gd ion, as can be seen in panel c of Fig. ???. Similar to the situation in AFM coupled ions on a triangular lattice, not all AFM exchanges can be simultaneously satisfied (i.e. by having completely antiparallel spins on each AFM bond). Each bond will then optimize the magnetic exchange energy together with the elastic energy resulting in bonds with antiparallel spins to contract whereas bonds with parallel spins will extend, as shown in Fig. ??(b). This can be understood from the dependence energy of each bond on the bond length between two Mn ions W , following Ref. [Harris1972], as:

$$W = J(r) \mathbf{S}_i \cdot \mathbf{S}_j + \frac{\kappa \delta r^2}{2r_0}, \quad (2.5)$$

with κ the elastic stiffness of the bond, r_0 the mean separation of Mn ions, spins \mathbf{S}_i and \mathbf{S}_j , and $\delta r = r - r_0$. Minimizing this bond energy (i.e. taking $\frac{\partial W}{\partial r} = 0$), leads to the change in bondlength δr upon condensing the magnetic structure to be given by

$$\delta r = -\frac{\partial J}{\partial r} \frac{r_0}{\kappa} \mathbf{S}_i \cdot \mathbf{S}_j. \quad (2.6)$$

If one then assumes that $J(r) = J_0 e^{-\frac{\varepsilon r}{r_0}}$ with ε some constant, the first order correction is given by

$$\delta r = J_0 \frac{\varepsilon}{\kappa} \mathbf{S}_i \cdot \mathbf{S}_j. \quad (2.7)$$

Thus, bonds with antiparallel spins will contract ($\delta r < 0$), and bonds with parallel spins will extend ($\delta r > 0$). In the RMn₂O₅ materials, this causes the octahedrally coordinated Mn⁴⁺ ion to shift towards one of the two neighbouring Mn³⁺ pyramids in the Mn³⁺ – Mn⁴⁺ – Mn³⁺ sequences, as showcased in Fig. ??(b). This leads to the lowering of the symmetry from Pbam to $P_a b2_1 a$, and, as the valence of the Mn³⁺ and Mn⁴⁺ ions differs, to a nonzero contribution to the polarization along the b -axis [Khomskii2009]. It was shown, however, that this ionic displacement is largely compensated by electronic correlation effects, shifting the electronic wavefunctions opposite to the ions and almost fully cancelling the contribution to the polarization that originates from the Mn chains. There is a second source of polarization in RMn₂O₅ with a magnetic rare-earth, also due to the symmetric Heisenberg exchange striction,

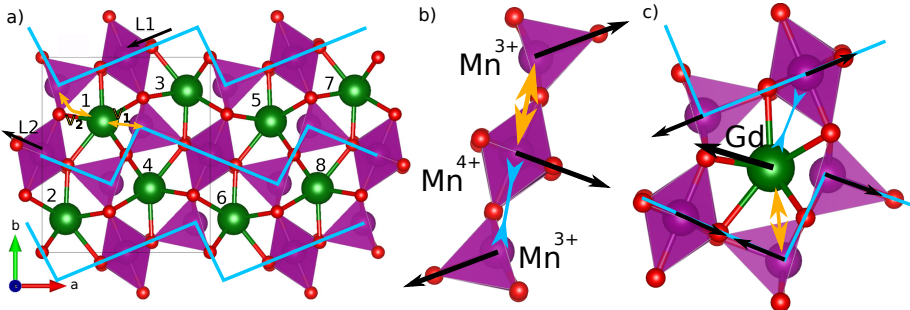


Figure 2.1: **Unit cell and magnetic configuration of GdMn_2O_5 .** The spheres signify Mn (purple), Gd (green) and Oxygen (red) ions. a) *Magnetic unit cell*, the zig-zag chains along the a -direction (cyan lines) show which Mn ions are linked with strong AFM exchange, resulting in the \mathbf{L}_1 and \mathbf{L}_2 Néel vectors. The boundary of the structural unit cell is marked by the black box and the yellow arrows denote the exchange paths between Gd and neighboring Mn ions in both chains, corresponding to v_1 and v_2 . (b-c) *Symmetric magnetostriction*, the black arrows signify the zero field orientation of the spins. The yellow arrows denote the expanding bonds due to alignment of spins and AFM exchange, and the blue arrows denote contracting bonds.

this time between the rare-earth and the surrounding Mn pentagon. A similar train of thought can be followed as before, where all the exchanges between the rare earth and the surround Mn ions are AFM, again causing certain bonds to have antiparallel spins versus parallel spins, and the associated contraction and extension (see Fig. ??(c)). This contribution does not suffer from the same cancellation between ionic displacements and electronic charge, and leads to the majority of the ferroelectric polarization in these materials.

Gd^{3+} is special with respect to the other magnetic rare-earths in $RM\text{n}_2\text{O}_5$, because it has a very isotropic electronic configuration ($4f^7$), i.e. there is no unquenched OAM and associated anisotropic charge distribution. This means that the large spin (nominally $S = 7/2$) can orient itself relatively freely to optimize the magnetic interactions with its neighboring Mn atoms, and that it has a high magnetic susceptibility and associated magnetoelectric effects. This leads to GdMn_2O_5 outclassing the other $RM\text{n}_2\text{O}_5$ compounds both in size and tunability of P_b , with a measured variation of up to $5000 \mu\text{C}/\text{m}^2$ when a magnetic field is applied [Lee13].

Now that the stage is set, we will describe the puzzling experimental observations that we will try to explain.

2.2 Experimental results

In previous experimental measurements, the magnetic field was always applied along the crystalline a -direction [Lee13]. This leads to the aforementioned reversal and restoration of the polarization, and a relatively normal hysteresis loop (see Fig. 1 of [Lee13]), alternating between two states. However, we found that the behavior of $P(H)$ depends strongly on the angle between the applied magnetic field and the a -direction, ϕ_H . As can be seen from Fig. ?? panel a, at

high angle P_b remains positive although a small jump can be observed signalling two different internal states. In the intermediate ‘magic angle’ region (panel b and d), there is a crossover between the low angle regime of Ref. ?? and the high angle regime of the experiments performed by the group of A. Pimenov, where four different states with different values of P_b are visited while the external field cycles up and down twice. This novel four state switching is the focus of this part of the thesis, and is found to originate from a rotational motion of the internal spins in one direction. One could say that this behavior is a microscopic analogy to the crankshaft in a car, converting the linear back-and-forth motion of the magnetic field into a unidirectional rotational motion of the spins. As will be shown below, these three regimes can each be assigned a winding number, with the four state switching regime lying on the boundary between the two extremal regimes. The topology of the parameter space in terms of ϕ_H is found to be such that this four state switching phase can be thought of as topologically protected, i.e. there always exists a region of ϕ_H where the four state cycle is present. The actual size of this region depends on the specific model parameters used, as will be discussed below. The results of the experiments performed on single crystal GdMn_2O_5 samples are shown in Fig. ???. As can be seen from the varying behaviors in panels (a-d), the evolution of P_b with $|H|$ is very dependent on its angle with the a -axis, ϕ_H . As alluded to before, at a certain magnitude of this angle and at low temperature, a peculiar deterministic four-state hysteresis loop develops. Even though all experimental measurements were performed on single crystal samples, the complexity and low symmetry of the material leads to a wealth of different effects, which is clear from the details of the P_b evolution at $T = 4K$, shown in panel e, but also from some details of the evolution at $T = 2K$. We will only focus on the overall behavior, i.e. how the main four-state regime develops as an interpolation between the high and low angle regimes that have the more usual two state switching loop. It is not clear what led to the discrepancy between the present low angle measurements (panel a) and earlier ones performed in Ref. [Lee13], from our theoretical model it will be shown that the behavior in Ref. [Lee13] arises, rather than the one observed here.

2.3 Modeling

In order to describe the physics at play we use a quasi-classical model Hamiltonian with eight Gd spins designated by unit vectors $\mathbf{S}_i, i = 1..8$, two AFM order parameters $\mathbf{L}_\alpha, \alpha = 1, 2$ (also unit vectors) given by the difference of spins of neighboring Mn ions inside the two Mn chains, and the slave order parameter P_b for the polarization, see Fig ???. Using these AFM order parameters amounts to taking the rigid spin approximation, i.e. all spins in each chain are assumed to be collinear with the same size and alternating sign. This simplification is justified by the large intrachain AFM exchanges, compared with the relatively small exchanges between the two chains. Another simplification that is adopted is to keep all spins in the ab -plane, since this was experimentally shown to be the case, and the layers couple ferromagnetically along the crystalline c -direction [Lee13]. This lowers the dimensionality of the problem from 3D to 2D, with a single angle per Gd spin and Mn chain as the remaining degrees of freedom, greatly simplifying the numerical solution. Since all spins and AFM order parameters are unit vectors, their sizes are implicitly included

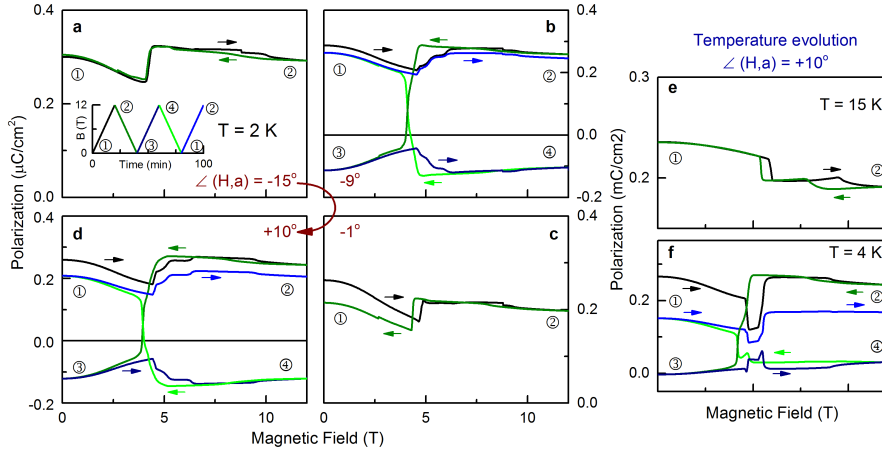


Figure 2.2: Evolution of the electric polarization loop across critical angle and critical temperature. (a) At higher temperatures only a small step is seen at the transition that shows some hysteresis and the two-state switching; (b) 4-state switching starts to appear approximately from $T = 5$ K. (c) four-state hysteresis loop is clearly seen at $T = 2.3$ K with the magnetic field at the “magic” angle; (d-f) Field dependence of the electric polarization of GdMn_2O_5 for different off-axis orientations of the applied magnetic field. (d,f): Conventional two-state switching is observed if magnetic field is (d) far away from the “magic” direction or (f) very close to the crystallographic a -axis. (e,g): Unusual four-state hysteresis loop for the magnetic field direction close to the magic angle of $\pm 9^\circ$. The inset shows the sequence of the magnetic field-sweeps. The labels 1-4 mark the four polarization states. The arrows show the direction of magnetic field-change during the sweep. The experiments have been done at $T = 2.3$ K.

in the model parameters.

The next step in deriving the appropriate model Hamiltonian using these simplifications and order parameters is to find symmetrically allowed combinations of them, which have to transform according to the unit representation of the symmetry group of the crystal. To this end we utilize the following symmetry operations of the paramagnetic high symmetry $Pbam$ phase:

$$I : (x, y) \rightarrow (-x, -y) \quad (2.8)$$

$$2z : (x, y) \rightarrow (-x, -y) \quad (2.9)$$

$$2y : (x, y) \rightarrow \left(\frac{1}{2} - x, \frac{1}{2} + y\right) \quad (2.10)$$

I and $2z$ are the same symmetry operations in the 2D case. Next, a doubling of the unit cell is necessary to fit the overall AFM magnetic state. This leads to additional symmetry operations when the spins are not taken into account, which in light of brevity we won’t fully enumerate here. For our purposes it suffices to write $2y : (x, y) \rightarrow (\frac{1}{4} - x, \frac{1}{2} + y)$ and add an additional symmetry operation $a : (x, y) \rightarrow (x + a, y)$. In effect, applying these symmetry operations to the degrees of freedom, bearing in mind the AFM spin transformation between the two halves of the magnetic unit cell, leads to the following transformation table:

| | S_1 | S_2 | S_3 | S_4 | S_5 | S_6 | S_7 | S_8 | L_1 | L_2 | P_b |
|----|-------|-------|-------|-------|-------|-------|-------|-------|--------|--------|--------|
| I | S_8 | S_7 | S_6 | S_5 | S_4 | S_3 | S_2 | S_1 | $-L_1$ | L_2 | $-P_b$ |
| 2y | S_4 | S_3 | S_2 | S_1 | S_8 | S_7 | S_6 | S_5 | L_1 | L_2 | P_b |
| a | S_5 | S_6 | S_7 | S_8 | S_1 | S_2 | S_3 | S_4 | $-L_1$ | $-L_2$ | P_b |

The first set of contributions are the Heisenberg exchange terms between the Gd spins and the Mn chains (L_1 and L_2), with the effective exchange parameters denoted by v_1 and v_2 . The former (latter) couples each Gd spin with the chain that harbors the closest (furthest) Mn ion. Starting from terms with S_1 and S_2 , taking into account the above table of transformations, the following sets of terms can be identified:

$$\begin{aligned} \mathbf{S}_1 \cdot (v_1 \mathbf{L}_2 + v_2 \mathbf{L}_1) &\xrightarrow{I} \mathbf{S}_8 \cdot (v_1 \mathbf{L}_2 - v_2 \mathbf{L}_1) \xrightarrow{a} \mathbf{S}_4 \cdot (-v_1 \mathbf{L}_2 + v_2 \mathbf{L}_1) \xrightarrow{I} \mathbf{S}_5 \cdot (-v_1 \mathbf{L}_2 - v_2 \mathbf{L}_1) \\ \mathbf{S}_2 \cdot (v_1 \mathbf{L}_1 + v_2 \mathbf{L}_2) &\xrightarrow{I} \mathbf{S}_7 \cdot (-v_1 \mathbf{L}_1 + v_2 \mathbf{L}_2) \xrightarrow{a} \mathbf{S}_3 \cdot (v_1 \mathbf{L}_1 - v_2 \mathbf{L}_2) \xrightarrow{I} \mathbf{S}_6 \cdot (-v_1 \mathbf{L}_1 - v_2 \mathbf{L}_2) \end{aligned} \quad (2.11)$$

The sum of all these contributions has the correct unit representation of energy, leading to the first contribution to the Hamiltonian:

$$\begin{aligned} H_{LS} = & \mathbf{S}_1 \cdot (v_1 \mathbf{L}_2 + v_2 \mathbf{L}_1) + \mathbf{S}_2 \cdot (v_1 \mathbf{L}_1 + v_2 \mathbf{L}_2) + \mathbf{S}_3 \cdot (v_1 \mathbf{L}_1 - v_2 \mathbf{L}_2) + \mathbf{S}_4 \cdot (-v_1 \mathbf{L}_2 + v_2 \mathbf{L}_1) \\ & - \mathbf{S}_5 \cdot (v_1 \mathbf{L}_2 + v_2 \mathbf{L}_1) - \mathbf{S}_6 \cdot (v_1 \mathbf{L}_1 + v_2 \mathbf{L}_2) - \mathbf{S}_7 \cdot (v_1 \mathbf{L}_1 - v_2 \mathbf{L}_2) - \mathbf{S}_8 \cdot (-v_1 \mathbf{L}_2 + v_2 \mathbf{L}_1) \end{aligned} \quad (2.12)$$

Since P_b is a scalar, a similar process can be applied starting from $P_b \mathbf{S}_1 \cdot (\beta_2 \mathbf{L}_1 + \beta_3 \mathbf{L}_2)$ and $P_b \mathbf{S}_2 \cdot (\beta_2 \mathbf{L}_1 + \beta_3 \mathbf{L}_2)$, which signify the symmetric Heisenberg magnetostriction contribution to the Hamiltonian. This leads to

$$\begin{aligned} H_{P_b} = & -P_b [E_b + \beta_1 (\mathbf{L}_1 \cdot \mathbf{L}_2) + (\mathbf{S}_1 - \mathbf{S}_5)(\beta_2 \mathbf{L}_2 + \beta_3 \mathbf{L}_1) + (\mathbf{S}_2 - \mathbf{S}_6)(\beta_2 \mathbf{L}_1 + \beta_3 \mathbf{L}_2) \\ & + (\mathbf{S}_3 - \mathbf{S}_7)(\beta_2 \mathbf{L}_2 - \beta_3 \mathbf{L}_1) + (\mathbf{S}_4 - \mathbf{S}_8)(\beta_2 \mathbf{L}_1 - \beta_3 \mathbf{L}_2)], \end{aligned} \quad (2.13)$$

where the dipole term from a possible external electric field $P_b E_b$ was also included. A further three terms in the Hamiltonian depend solely on L_1 and L_2 :

$$H_L = \Gamma (\mathbf{L}_1 \cdot \mathbf{L}_2)^2 + \sum_{\alpha} \chi^{-1} ((\mathbf{H} \cdot \mathbf{L}_{\alpha})^2 - H^2) - K_L \sum_{\alpha} (\mathbf{L}_{\alpha} \cdot \mathbf{n}_{\alpha})^2 \quad (2.14)$$

The first originates from the gain in exchange energy through spin canting when the chains are not colinear, due to the competition of interchain exchange J_{\perp} and the intrachain AFM exchange $J_{||}$ [Sushkov2008] [more details?], with $\Gamma \sim \frac{J_{\perp}^2}{J_{||}} > 0$. The term with χ represents the gained Zeeman energy when the Mn spins are slightly canted from the purely AFM order inside the chains, resulting in a weak magnetic moment which couples to the external field. The last denotes the easy-axis anisotropy which is aligned with the fourfold axes of the pyramidal coordinated Mn ions, i.e. $\mathbf{n}_{\alpha} = (\cos(\pm 23.4^\circ), \sin(\pm 23.4^\circ))$ respectively.

Similarly, three terms can be identified as coming purely from the Gd spins:

$$H_S = \frac{1}{2} (g\mu_B)^2 \sum_{i \neq j} \left(\frac{\mathbf{S}_i \cdot \mathbf{S}_j}{r_{ij}^3} - 3 \frac{(\mathbf{S}_i \cdot \mathbf{r}_{ij})(\mathbf{S}_j \cdot \mathbf{r}_{ij})}{r_{ij}^5} \right) - \sum_i (K_S (\mathbf{N}_i \cdot \mathbf{S}_i)^2 + g\mu_B \mathbf{H} \cdot \mathbf{S}_i) \quad (2.15)$$

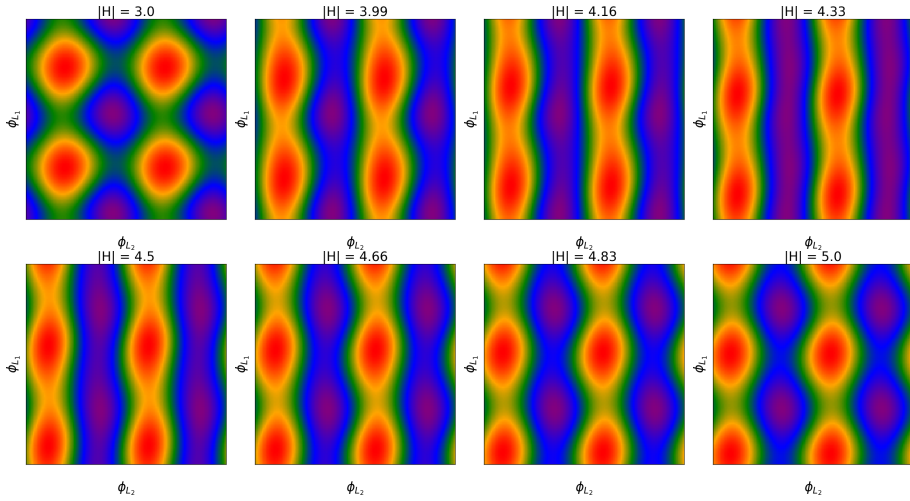


Figure 2.3: **Energy surfaces inside hysteresis loop** ϕ_{L_1} and ϕ_{L_2} both range between 0 to 2π .

The first describes the magnetodipolar interaction between Gd spins, which could be relatively large due to the size of the spins and relative proximity to the neighbors. In the numerical simulations these were restricted to five nearest neighbors, including periodic images. Including further neighbors did not lead to qualitative differences of the results. Again an anisotropy term is included, this time with anisotropy axes N_i , unit vectors alternating as $\pm 12^\circ$. K_S is significantly smaller than K_L due to the isotropic environment and spin configuration of the Gd ions. The final term denotes the Zeeman energy from the interaction with the externally applied magnetic field.

The model parameters used here are $J_\perp = 1.89$ meV, $J_\parallel = 26.67$ meV, $K_L = 5.27$ meV, $K_S = 0.2$ meV, $v_1 = 3.33$ meV, $v_2 = 0.15$ meV [check order parameters, maybe show different sets?]. with the model parameters used to fit the experimental data, $\alpha = 0.06 \mu\text{C}/\text{cm}^2$, $\beta = 0.04 \mu\text{C}/\text{cm}^2$, $\gamma = 0.06 \mu\text{C}/\text{cm}^2$.

As mentioned before, the low temperature commensurate state breaks both time reversal symmetry, $T : (\mathbf{L}_1, \mathbf{L}_2) \rightarrow (-\mathbf{L}_1, -\mathbf{L}_2)$, and inversion symmetry $I : (\mathbf{L}_1, \mathbf{L}_2) \rightarrow (-\mathbf{L}_1, \mathbf{L}_2)$, which makes the system fall into one of the fourfold degenerate energy minima as shown in the top left panel of Fig. ???. To simulate the experimental measurements in Fig. ?? at low temperature, we choose one of the four degenerate minima of the Hamiltonian, gradually increase and decrease the applied magnetic field, and minimize the energy in order to track the instantaneous local minimum.

The results are shown in Fig. ??

In order to understand the energy surface connecting the four states, we proceed by labeling them in the same way as Fig. ??, and perform a nudged elastic band calculation between the four states at a given magnetic field inside the hysteresis region. This results in the evolution of barriers between these states as shown in panel (g), where the color coding is used to denote the magnetic field strength, and the energy graphs are offset for clarity. The arrows and blue balls denote the evolution during the double magnetic field sweep. As expected, two minima with opposite P_b are degenerate each value of H , at

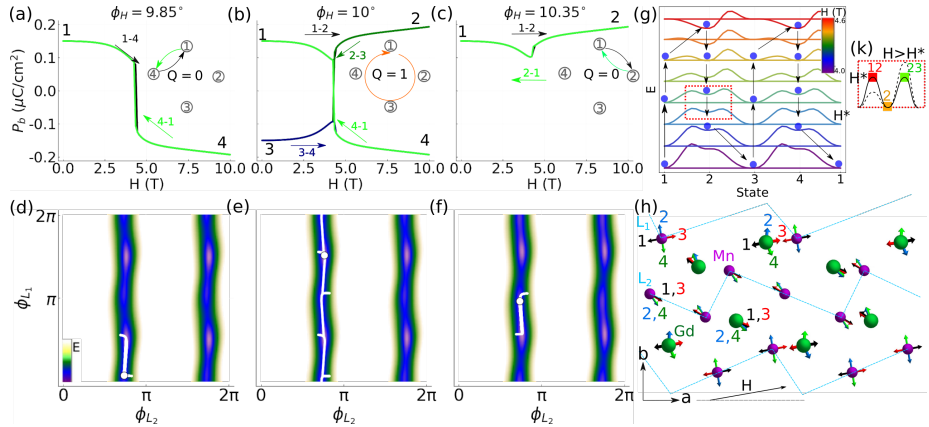


Figure 2.4: Simulation of magnetoelectric behaviour. (a-c) Evolution of electric polarization P_b during the magnetic field sweep cycle for various magnetic field orientations. In each panel, the changes of the curve color indicate the same progression of the sweep cycle as Fig 2. The four-state switching is seen for the field at the magic orientation. The insets indicate the corresponding switching paths and winding numbers. (d-f) Trajectories (in green) in the space of the Néel vectors orientations, (ϕ_{L_1}, ϕ_{L_2}) , through the field sweep cycles in different regimes. The color map shows the energy landscape in the vicinity of the switching fields. (g) Evolution of transition barriers between states 1,2,3,4 as the magnetic field at 10° to the a axis is swept through the hysteresis region. The plots are shifted vertically, and magnetodipolar interactions were enhanced by a factor of 5.3 for clarity. The curve colors encode the corresponding magnetic field strength. The trajectory of the energy minimum due to field sweeps is shown with blue circles and arrows. Coordinated changes of the state energies and barrier asymmetry with magnetic field enable the topological behavior. (h) Spin configurations in states 1, 2, 3 and 4. (k) Schematic evolution of the barriers connecting the state 2 to states 1 and 3 in the vicinity of H^* . Saddle point states are denoted by 12 and 23.

low field these are located at states 1 and 3, then as the field is ramped up they move to favor states 2 and 4. We see that during the sweep the barriers between the different states evolve asymmetrically. Starting in state 1, when the field is ramped up the barrier towards state 2 decreases faster than the one towards state 4, causing the system to move from 1 to 2. Then, as the magnetic field is lowered again, the barrier from 2 to 3 increases slower than from 2 to 1. When ultimately state 2 goes from being metastable to a saddle point, the system spills over towards state 3, and so on. In order to try and understand where the asymmetric evolution of the barriers comes from, we investigate the situation around the particular H -field strength where the system is close to state 2, and the barriers between state 2 and 1, and 2 and 3 are the same height. This situation is highlighted by the red dashed box around the blue graph in Fig. ??(g). The inset of panel (k) provides a zoom on the energy surface. The states 12 and 23 denote the configurations on top of the barriers from 1 to 2 and 2 to 3, respectively. A Taylor expansion in terms of H , around

H^* can be performed for both states:

$$F(H) = F(H^*) + \frac{\partial F}{\partial H} \Big|_{H=H^*} (H - H^*) + \dots \quad (2.16)$$

If one then subtracts the results, using $\frac{\partial F}{\partial H} = M$, the following expression is found

$$E_{12}(H) - E_{23} \sim (M_{12} - M_{23})(H - H^*). \quad (2.17)$$

This means that, to first order, the evolution of the barrier asymmetry is given by the difference in magnetization of the two states on top of the barriers. The magnetization of both states can be calculated using the following formula

$$\mathbf{M} = -\frac{\partial F}{\partial \mathbf{H}} = \sum_i g\mu_B \mathbf{S}_i - \sum_\alpha 2\chi^{-1} \mathbf{L}_\alpha (\mathbf{H} \cdot \mathbf{L}_\alpha) \quad (2.18)$$

Indeed we find that the magnetizations are different from our simulations, $M_{23} > M_{12}$, confirming that this is at least a part of the reason for the asymmetric evolution of the barriers. Moreover, due to the symmetry of the system, this asymmetry is opposite when the field is swept up, as compared with when the field is swept down. This causes that when $H > H^*$ the barrier from state 1 to state 2 lowers faster than the one towards state 4, and by symmetry, the barrier from state 3 to state 4 lowers faster than from state 3 to 2. The converse is true when $H < H^*$, but since the system is then coming from the high-field configurations, it moves from 2 to 3 and 4 to 1 rather than the opposite direction. This causes the deterministic unidirectional movements through the four states sequentially when two field sweeps are applied. Since the two low field states that get accessed sequentially have two different P_b values, this situation effectively results in a single crystal binary counter behavior.

The magnetic configuration of the four extremal states is displayed in panel (h) of the same figure, showcasing the rotational motion of the spins inside the chain most parallel to the applied magnetic field, and the Gd ions coupled most strongly with it. This robust one directional rotation allows us to assign a non-zero winding number to the ‘magic-angle’ switching behavior, i.e. $Q = \frac{1}{2\pi} \int_0^{T_0} dt (L_x \partial_t L_y - L_y \partial_t L_x)$.

2.4 Simplified Model

Having found a description for the situation in the complicated material GdMn_2O_5 using the model ??, one may wonder what the minimal requirements are to have a similar four-state behavior where the spins rotate 360° while the applied field only oscillates back and forth along a single axis. We look to the spin configurations of Fig. ??(h) for inspiration. It is clear that, although both chains are necessary for the P_b behavior, the chain with equilibrium Mn moments most parallel to the applied field does the full rotation, while the other chain merely oscillates around its starting position. Similarly, only the Gd moments most strongly coupled to that chain perform the full 360° cycle. This warrants an attempt to search for the four state behavior using only a single chain with its Gd moments, more specifically, in the case of $\phi_H = +10^\circ$, we keep L_1, S_2, S_3, S_6 and S_7 as the degrees of freedom in the model. Given the negligible importance of the anisotropy on the Gd ions, we also put $K_S = 0$. This leaves us with

the following Hamiltonian, which is split up in two parts, one with the dipolar terms H_{dip} and one with all the other terms H' :

$$H = H' + H_{dip} \quad (2.19)$$

$$H' = v_1(\mathbf{S}_2 + \mathbf{S}_3 - (\mathbf{S}_6 + \mathbf{S}_7)) \cdot \mathbf{L}_1 - g\mu_b(\mathbf{S}_2 + \mathbf{S}_3 + \mathbf{S}_6 + \mathbf{S}_7) \cdot \mathbf{H} \quad (2.20)$$

$$- K_L(\mathbf{L}_1 \cdot \mathbf{n})^2 \quad (2.21)$$

$$H_{dip} = \frac{1}{2}(g\mu_B)^2 \sum_{i \neq j} \left(\frac{\mathbf{S}_i \cdot \mathbf{S}_j}{r_{ij}^3} - 3 \frac{(\mathbf{S}_i \cdot \mathbf{r}_{ij})(\mathbf{S}_j \cdot \mathbf{r}_{ij})}{r_{ij}^5} \right). \quad (2.22)$$

Due to the higher symmetries of this model throughout the field sweep cycle, compared with the full model, one can identify two symmetry related copies of one spin in the first half of the magnetic unit cell and one in the second half of the unit cell, with the chain in between (see Fig. ??), i.e. $S_2 = S_3$ and $S_6 = S_7$. This further simplifies the Hamiltonian:

$$H' = 2v_1(\mathbf{S}_3 - \mathbf{S}_6) \cdot \mathbf{L}_1 - 2g\mu_b(\mathbf{S}_3 + \mathbf{S}_6) \cdot \mathbf{H} \quad (2.23)$$

$$- K_L(\mathbf{L} \cdot \mathbf{n})^2 \quad (2.24)$$

$$H_{dip} = (g\mu_B)^2 \left(\frac{\mathbf{S}_3 \cdot \mathbf{S}_6}{r_{36}^3} - 3 \frac{(\mathbf{S}_3 \cdot \mathbf{r}_{36})(\mathbf{S}_6 \cdot \mathbf{r}_{36})}{r_{36}^5} \right). \quad (2.25)$$

[what can we say more about this?]

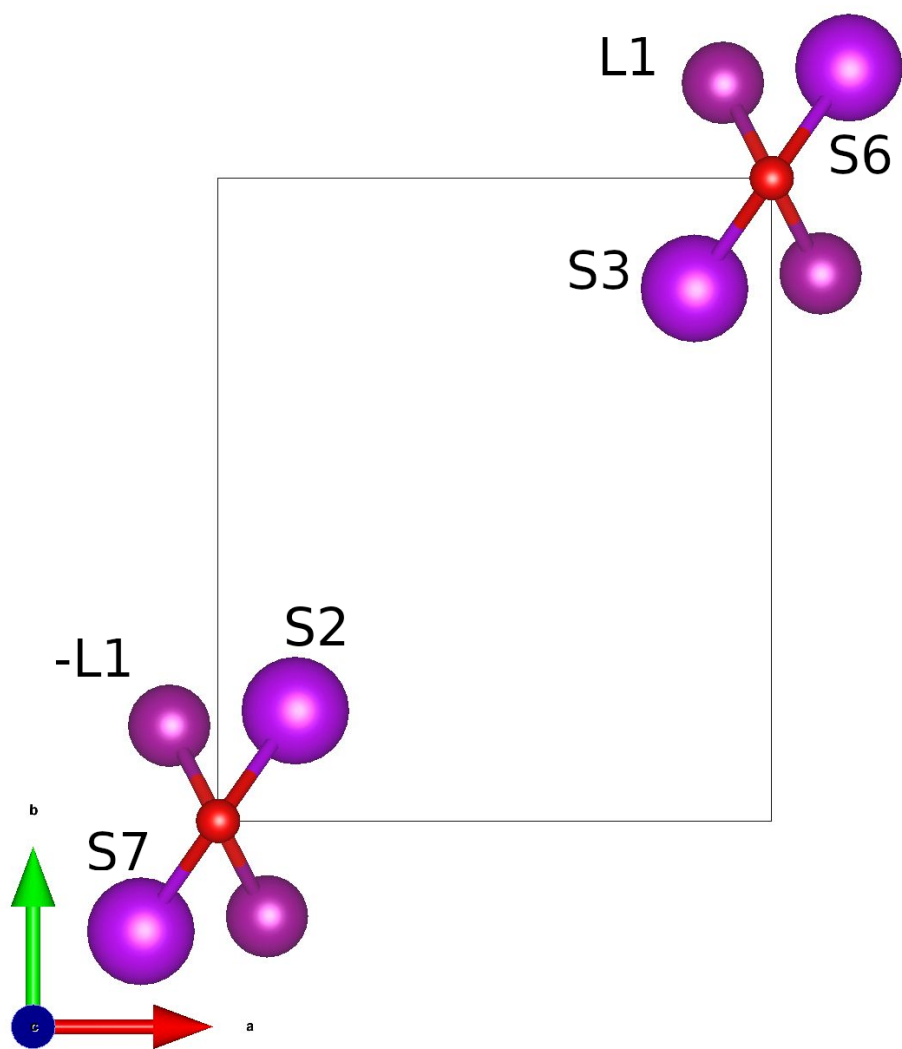


Figure 2.5: Simplified single chain model.